Cement & Concrete Composites 32 (2010) 678–685

Contents lists available at ScienceDirect

Cement & Concrete Composites

journal homepage: www.elsevier.com/locate/cemconcomp

Experimental and micro-mechanical analysis of the mechanical and transport properties of mortar containing heat-induced micro-cracks

Xiao-Ting Chen [a], C.A. Davy [a], J.F. Shao [b,*], F. Skoczylas [a]

[a] Laboratoire de Mécanique de Lille (LML), UMR 8107, and Ecole Centrale de Lille, BP 48, F-59651 Villeneuve d'Ascq Cedex, France
[b] Laboratoire de Mécanique de Lille (LML), UMR 8107, and Polytech'Lille, Bd P. Langevin, F-59650 Villeneuve d'Ascq, France

ARTICLE INFO

Article history:
Received 19 March 2009
Received in revised form 20 July 2010
Accepted 21 July 2010
Available online 30 July 2010

Keywords:
Mortar
Concrete
Thermal damage
Micro-cracks
Pore collapse
Micromechanics

ABSTRACT

This paper focuses on the effect of micro-cracks induced by a slow heating/cooling process (also called heat-treatment) in a mortar, upon its poro-elastic properties under drained hydrostatic compression, and upon its intrinsic permeability. Prior to the experiments, mortar samples are subjected to a slow heating-cooling cycle up to one temperature $T = 105$, 200, 300 and 400 °C. The reference state of mortar is taken after drying at 60 °C until constant mass. Experimental results show that the effective drained bulk modulus K_b of mortar decreases significantly with heat-treatment temperature T. A transition from elastic to plastic behavior with increasing heat-treatment temperature T is also observed. These effects are mainly attributed to heating-induced micro-cracks, and, to a lesser extent, to the increase in connected porosity. We also measure a significant increase in permeability.

Based on these experimental evidences, a micro-mechanical analysis is proposed, which describes micro-cracks as independent 3D penny-shaped cracks of varying aspect ratio α. A relationship between the degradation of bulk modulus and heating-induced micro-cracks is established. The distribution of aspect ratio of micro-crack porosity is determined for each heat-treatment temperature. The correlation between heating-induced crack porosity (or with crack aspect ratio) and permeability is also determined. Finally, a phenomenological law is proposed to describe the increase in plastic deformation with T. Good correlation with experimental stress–strain curves is found.

1. Introduction

Cement-based materials may be subjected to high temperatures (i.e. above 100 °C) in normal service conditions, such as in nuclear power plants, radioactive waste storage facilities, or under accidental conditions, for instance during fire incidents in buildings and tunnels. Temperature variations and heating/cooling cycles may also be encountered. In such circumstances, physical transformations and chemical decompositions occur [1], leading to significant degradation of material properties and seriously affecting material durability. It is generally acknowledged that high temperature increase generates significant modifications in pore microstructure [2], nucleation and propagation of micro-cracks [3–5], and cement paste dehydration or decarbonation [6]. Cooling also causes additional micro-cracking, although to a lesser extent than heating [7]. In particular, during cooling from 620 °C, lime CaO contained in cement paste expands upon rehydration, when forming back portlandite [8], and this phenomenon is bound to generate micro-cracking. As a consequence, at the macroscopic scale, the mechanical behavior of cement-based materials is affected by heating and cooling with, for instance, diminution of elastic modulus, reduction of mechanical strength and plastic yield threshold. Further, heating and cooling also affect material porosity and permeability, as reported in [9–12].

Both mechanical and fluid transport behaviors of micro-cracked porous materials may be predicted at the sole macroscopic scale. Following numerous works [13–15], the most common approach is to introduce a damage parameter D, either scalar (for an isotropic medium) or as a tensor (for an anisotropic medium), into the mechanical constitutive equations. Damage D describes the effect of concrete micro-cracking, both mechanically and thermally induced. Such approach may also be coupled to the prediction of fluid transport properties in presence of micro-cracks. In such instance, damage D is generally related to permeability using empirical relationships [15–17]. Most interestingly, Dal Pont et al. [15] relate intrinsic permeability K_{int} of an industrial concrete *under temperature* to its sole damage level D: experimental validation of their numerical model shows that the influence of gas pressure and temperature upon K_{int} is negligible, contrarily to that of damage D.

Let now a microstructure scale be considered. When heat-treated cement-based materials are subjected to compressive stresses,

---

[*] Corresponding author. Tel.: +33 3 20 43 46 26; fax: +33 3 20 33 71 53.
E-mail address: jian-fu.shao@polytech-lille.fr (J.F. Shao).

0958-9465/$ - see front matter © 2010 Elsevier Ltd. All rights reserved.
doi:10.1016/j.cemconcomp.2010.07.016

heating-induced micro-cracks close progressively, provided their opening is parallel to the loading direction. This results in nonlinear mechanical response [18,19]. At the microscopic scale, such response is affected by the distribution of micro-cracks and pores, in relation with their density, size and shape (or aspect ratio), and orientation [18,20]. Micro-mechanical approaches propose relationships between micro-crack distribution and macroscopic response. These are determined through varied nonperiodical homogenization methods depending on the morphology of heterogeneities [20–23,18]. In particular, the dilute scheme assumes no interaction between cracks, which is adapted for small micro-crack amounts. On the opposite, the self-consistent scheme takes into account crack interactions together with a disordered heterogeneity distribution, and it is adapted to more important micro-crack densities. In the framework of a micro-mechanical model based on the self-consistent scheme, Dormieux et al. [20] have described permeability evolution in relation with micro-crack density and mechanical loading.

The present work is devoted to the experimental investigation and to the micro-mechanical analysis of micro-cracks induced by a heating/cooling process: except in the reference state (drying at 60 °C until constant mass), mortar is subjected to a heat-treatment up to T = 105, 200, 300 and 400 °C. Hydrostatic compression tests are performed, in order to study the evolution of the effective drained bulk modulus K_b with heat-treatment temperature T and confining pressure P_c. Intrinsic gas permeability K_{int} is also assessed. The evolution of drained bulk modulus K_b is analyzed using a micro-mechanical model, which takes into account a uniform distribution of penny-shaped micro-cracks, mainly characterized by their aspect ratio α and density Γ, and which closure is sensitive to confinement. At each heat-treatment temperature T, we provide numerical predictions of micro-crack porosity ϕ, of micro-crack porosity distribution $d\phi/d\alpha$ and of micro-crack density distribution $d\Gamma/d\alpha$ in relation with aspect ratio α. Correlation between intrinsic gas permeability and micro-crack porosity is determined, and macroscopic plastic strain is predicted in order to reproduce experimental stress strain curves (ε_v,P_c).

2. Experimental investigation: methods and results

2.1. Materials and thermal cycling

A normalized mortar, with a water-to-cement (W/C) ratio of 0.5, is used in this work. Mortar is prepared in one batch with pure silica sand (from Leucate, France) and Type II cement powder (CEM II/B-M (LL-S) 32.5 R). It is matured in lime-saturated water at 20 °C for 6 months. Then, samples of the first series have been cored and ground to 37 mm diameter and 70 mm height, whereas three samples, of the second series, heve been cored to 65 mm length and 70 mm height. Results for the first series of specimens (confined up to 25 MPa) is presented in [11], whereas those for the second series (tested up to 60 MPa) are original.

All samples are initially dried under 60 °C until constant mass. Following different former works [24–26], this state is considered as a reference state for mortar, because free water is evacuated from macro-pores, without significantly damaging the C–S–H gel.

Except for the reference ones, specimens are heated up to a temperature T of 105, 200, 300 and 400 °C, and then cooled down to ambient temperature. The lower heat-treatment temperature of 105 °C was chosen because C–S–H dehydration is shown to start from this temperature, above free water evaporation. Following former works [27,28], the rate of temperature change is kept constant and as low as at 20 °C/h during both heating and cooling periods, in order to ensure a uniform temperature within the sample, given its size. This also aims at avoiding any thermal shock. For similar reasons, when T is reached, samples are maintained at this temperature for 1 h. The total number of specimens tested after heat-treatment up to T is provided in Table 1. The second series of specimens for poro-mechanical testing (with a 65 mm diameter and a 60 mm length) comprises one in the intact state (after 60 °C drying), and two after heat-treatment up to 400 °C. The first series of poro-mechanical tests has been presented and discussed in [11], whereas all permeability results and poro-mechanical results of the second series are original to this contribution. On average, at each heat-treatment temperature T, two samples have been used for poro-mechanical assessment or for gas permeability measurement.

2.2. Experimental procedures

Hydrostatic compression tests and permeability measurements are performed using a hydrostatic pressure cell, see [11] for details. Hydrostatic pressure (or confining pressure) P_c is generated and controlled by an oil pump with an accuracy of ±(1/4) MPa. During gas permeability measurements, interstitial pressure is controlled and monitored by two manometers located at both sample ends, with an accuracy of ±0.1 MPa. Argon U of above 99% purity is used instead of water as the injected fluid, in order to avoid chemical interactions with cement paste. Inside the cell, the sample is sealed from the confining pressure oil with a rubber jacket.

Four strain gauges located at mid-height of the sample, provide two longitudinal and two transversal strain measurements (ε_{l1}, ε_{l2}) and (ε_{t1}, ε_{t2}) at an accuracy of $\pm 10^{-6}$. Assuming that the material is isotropic, volumetric strain ε_v is directly calculated as three times the average value of the four gauge measurements: $\varepsilon_v = 3\frac{\varepsilon_{l1}+\varepsilon_{l2}+\varepsilon_{t1}+\varepsilon_{t2}}{4}$. All tests are performed in a temperature-controlled room at 22 °C, in order to avoid thermal effects on confining and interstitial pressures, and also on strain gauge measurements.

Hydrostatic compression tests are performed in drained condition with a number of unloading-reloading cycles. The drained bulk modulus K_b is evaluated upon one unloading cycle ΔP_c of 5 MPa. We assume that such a small unloading corresponds to the release of elastic energy only, so that the determination of K_b is performed in the elastic domain. The pore (or interstitial) pressure P_i remains constant while confining pressure is changed by ΔP_c. Drained bulk modulus K_b is then calculated by [29]:

$$K_b = -\frac{\Delta P_c}{\Delta \varepsilon_v} \tag{1}$$

where $\Delta\varepsilon_v$ is the corresponding change in volumetric strain ($\Delta\varepsilon_v < 0$ denotes volumetric compaction).

Gas permeability measurements are performed at a fixed confining pressure P_c of 5, 12, 15 or 25 MPa, At the lower confinement of 5 MPa, a majority of heating-induced micro-cracks is assumed open. Intrinsic permeability is calculated after correction of Klinkenberg effects, see [30,31].

2.3. Experimental results and analysis

For the first series of hydrostatic tests upon reference mortar and mortars heat-treated up to 105, 200, 300 and 400 °C, stress strain curves (ε_v,P_c) have been presented and discussed extensively in [11]. Fig. 1 presents the mechanical behavior of both a reference sample, and two 400 °C heat-treated samples, one from the first series of tests, the other (tested up to 60 MPa) from the second series. Such comparison between two test series highlights the good test reproducibility, with very limited difference in the stress–strain curves of the two 400 °C heat-treated samples. Stress–strain curves of reference samples of the two series are superposed (not represented).

Table 1
Main characteristics of all experimental test series performed on heat-treated mortar, either for poro-mechanical assessment under drained conditions, or for gas permeability measurement.

Maximum temperature T (°C)	Number of samples tested	Maximum hydrostatic pressure P_c (MPa)	Type of test
60	3 (first series)	25	Poro-mechanical
	1 (second series)	60	Poro-mechanical
	2		Gas permeability
105	2	25	Poro-mechanical
	2		Gas permeability
200	2	25	Poro-mechanical
	2		Gas permeability
300	2	25	Poro-mechanical
	2		Gas permeability
400	2 (first series)	25	Poro-mechanical
	2 (second series)	60	Poro-mechanical
	2		Gas permeability

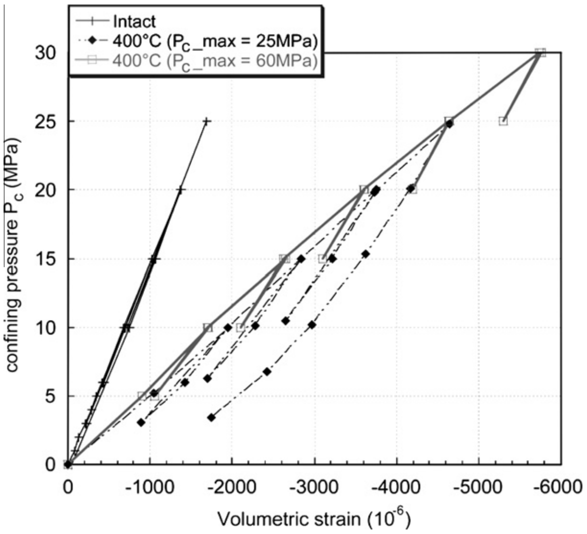

Fig. 1. Stress–strain curve (ε_v,P_c) for reference mortar and for two samples heat-treated up to 400 °C: samples tested up to 25 MPa belong to the first series, and have been previously presented in Chen et al. [11], whereas sample tested up to 60 MPa (partial result up to 30 MPa confinement) belongs to the second series and is original.

Fig. 1 shows that the overall mechanical response of mortar is strongly affected by the level of heat-treatment temperature T. For intact mortar, the stress–strain curve (ε_v,P_c) is almost linear, and there is no plastic strain upon unloading. This is similar for heat-treatments at 105 °C. On the opposite, for samples heat-treated up to 200–400 °C, the stress–strain curve (ε_v,P_c) is strongly nonlinear; important plastic strain is obtained after unloading. The overall deformability is much higher than that of the intact material (it is about three times higher for 400 °C heat-treatment). The strong nonlinearity of (ε_v,P_c) after 400 °C heat-treatment is attributed to two mechanisms: the progressive closure of heating-induced micro-cracks, and the plastic pore collapse by gradual failure of solid skeleton bridges. Similar phenomena have been observed in other porous materials, such as porous chalk ([32]).

Let consider now the variations of drained bulk modulus K_b with T and P_c, see Table 2 and Fig. 2. Fig. 2 plots the variations of drained bulk compressibility for $C_{bc} = (1/K_b)$ (inverse of drained bulk modulus) with confining pressure for different heat-treatment temperatures. Numerical fitting is also provided for comparison purpose, yet it will be detailed in next section.

Table 2
Main experimental results of drained bulk modulus K_b with varying heat-treatment temperature T and hydrostatic pressure P_c. Results are averaged on all samples tested at given T, see Table 1 for their exact quantity.

Maximum heat-treatment temperature T (°C)	Hydrostatic pressure P_c (MPa)	Average drained bulk modulus $K_{b\ mean}$ (MPa)	Distance to the average (% of average)
60	12	16,300	5
	15	16,120	4.6
	20	16,260	6.5
	25	16,520	5.1
105	12	16,110	1
	15	16,190	0.6
	20	15,890	0.3
	25	16,240	0.2
200	12	13,240	6.5
	15	12,850	2.5
	20	13,080	1.8
	25	13,730	1.3
300	12	9140	8.5
	15	9840	5.8
	20	10,260	5.3
	25	11,220	3.8
400	12	7630	3.8
	15	8980	4.2
	20	9540	3.5
	25	10,250	5.7
	30	10,660	6
	35	11,320	4.6
	40	11,950	4.5
	45	12,670	–
	50	13,280	–
	60	14,400	–

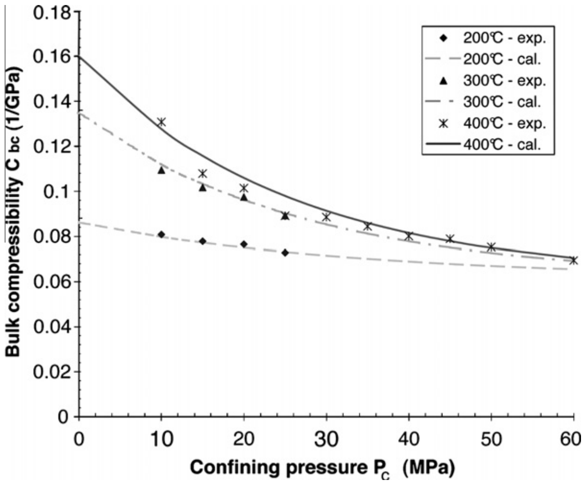

Fig. 2. Bulk compressibility curves $\left(C_{bc} = \frac{1}{K_b}\right)$ for mortar treated at different temperatures: numerical fitting (continuous lines) and test data (points).

We can see that the value of initial bulk compressibility C_{bc} (asymptotic value when confining pressure vanishes to zero) significantly increases with heat-treatment temperature T. This indicates the growth of micro-cracks during the heating/cooling process. However, the increase of bulk compressibility (or bulk modulus K_b) due to heating/cooling becomes significant only when T is strictly higher than 105 °C, see Table 2: this justifies that results at 105 °C are not used in the micro-mechanical analysis (see next section).

During hydrostatic compression tests, the bulk compressibility C_{bc} progressively decreases (i.e. K_b increases), as a consequence of progressive closure of micro-cracks and of a portion of pores. For instance, for $T = 400$ °C, K_b is 7630 MPa (on average) at $P_c = 12$ MPa; it is nearly multiplied by 2 with a value of 14,400 MPa at $P_c = 60$ MPa. For T lower than 200 °C, the decrease of bulk compressibility C_{bc} is negligible, and the mechanical behavior of mortar is nearly linear: C_{bc} may be considered as a constant. For instance, intact mortar (dried at 60 °C) has a nearly constant value for K_b, which is 16,300 MPa on average, see Table 2. This means that there exists some limit temperature below which the heat-treatment process does not induce micro-cracks and modify the pore network. Further, it is observed that, for the two samples heated up to 400 °C (second series), the value of bulk modulus at $P_c = 60$ MPa is very close to that of the intact sample (i.e. 16,300 MPa), although a bit smaller. This indicates that the heat-induced micro-cracks are almost closed when applying a hydrostatic stress as high as 60 MPa. The small difference between the two values may be attributed to the coarsening of pores, and/or to chemical degradation of solid skeleton bridges (due to the severe heating process up to 400 °C).

In Fig. 3a and b, the variation of intrinsic permeability of mortar K_{int} is presented as a function of heat-treatment temperature T and confining pressure P_c. We clearly see that K_{int} increases monotonously with T, in good correlation with the increase of bulk compressibility C_{bc} due to the growth of micro-cracks. On the opposite, K_{int} decreases with increasing P_c, due to the progressive closure of larger and larger micro-cracks. Table 3 also provides permeability results for each heat-treatment temperature T, with increasing confinement P_c. All values presented are averages, and, in all cases, the distance to each average represents less than 10% of the average. Due to this limited distance to the average, test representativity is considered good.

Table 3
Main experimental results of intrinsic gas permeability K_{int} with varying heat-treatment temperature T and hydrostatic pressure P_c. Results are averaged on all samples tested at given T, see Table 1 for their exact quantity. All distances to the averages provided are less than 10% of each average.

Temperature (°C)	Intrinsic permeability K_{int} (m^2)			
	$P_c = 5$ MPa	$P_c = 12$ MPa	$P_c = 15$ MPa	$P_c = 25$ MPa
60	6.3×10^{-18}	6.0×10^{-18}	6.3×10^{-18}	5.8×10^{-18}
105	6.5×10^{-18}	6.2×10^{-18}	6.2×10^{-18}	6.0×10^{-18}
200	1.8×10^{-17}	1.6×10^{-17}	1.6×10^{-17}	1.4×10^{-17}
300	6.8×10^{-17}	6.1×10^{-17}	5.7×10^{-17}	5.1×10^{-17}
400	2.4×10^{-16}	2.1×10^{-16}	2.1×10^{-16}	1.8×10^{-16}

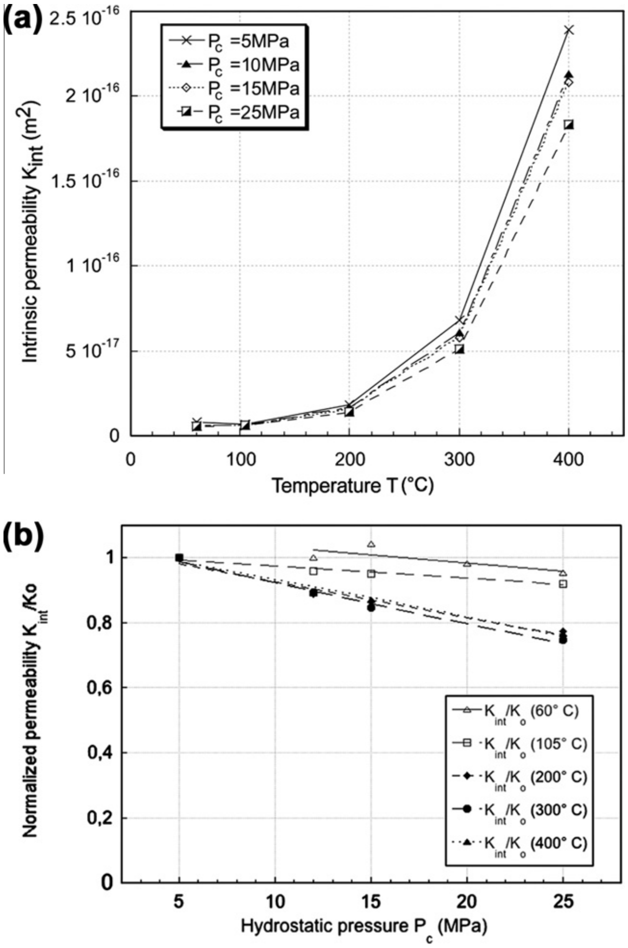

Fig. 3. Variation of (a) average intrinsic permeability K_{int} with heat-treatment temperature T and (b) normalized intrinsic permeability K_{int}/K_0 with hydrostatic stress P_c, where $K_0 = K_{int}(P_c = 5\text{ MPa})$.

3. Micro-mechanical analysis

In this section, a micro-mechanical analysis of heating-induced micro-cracks is proposed, based on the model by Zimmerman [18] which is limited to hydrostatic compressive loading. This micro-mechanical model is based on the classical dilute homogenization scheme [33]. First, we determine the distribution of micro-crack porosity with respect to aspect ratio α, in relation with heat-treatment temperature T, by using the evolution of effective bulk compressibility C_{bc}. Secondly, we analyze whether intrinsic permeability K_{int} correlates with crack porosity ϕ.

3.1. General assumptions

Reference mortar, dried up to 60 °C only, is considered devoid of micro-cracks: it is only a porous isotropic, homogeneous, linear elastic medium. On the opposite, heat-treated mortar is considered as a homogeneous medium, made of a linear elastic and isotropic solid matrix identical to that of reference mortar, but also containing N 3D oblate ellipsoids (also called *penny-shaped cracks*) within a total bulk volume V_b, each having a semi-major axis a and a semi-minor axis c. An isotropic distribution of penny-shaped cracks is assumed. Initial crack aspect ratio is defined by $\alpha = c/a \ll 1$. In the case of hydrostatic loading as solely considered here, cracks are assumed to have the same radius a, so that a crack family is completely defined by its initial aspect ratio α. With these assumptions, the closure of micro-cracks during hydrostatic compression is only controlled by the aspect ratio: when $\alpha = 0$, micro-cracks of aspect ratio α are closed.

Should a different stress state be considered, cracks are also defined by a unit normal vector indicating their orientation, and a more general approach for this is proposed by Dormieux et al. [34]. In the case of uniaxial compression, the distribution of crack-density with respect to aspect ratio is determined in [19].

In the present case (hydrostatic compression), the crack porosity ϕ is given by ([18]):

$$\phi = \frac{N}{V_b}\frac{4\pi a^2 c}{3} = \frac{4\pi N a^3 \alpha}{3V_b} = \frac{4\pi\alpha}{3}\Gamma \tag{2}$$

where $\Gamma = Na^3/V_b$ is a dimensionless crack-density parameter. In the present work, we assume that crack-density in mortar is relatively small and interactions between cracks are neglected. This allows to use the dilute homogenization scheme to change scale, from that of cracks and solid matrix, to the macroscopic scale, see next subsection.

By definition, the crack-density (number) of cracks whose aspect ratio is in the range α to $\alpha + d\alpha$ is given by $d\Gamma = (d\Gamma/d\alpha) = -\gamma(\alpha)d\alpha$, where $\gamma(\alpha) = -(d\Gamma/d\alpha)$ is the aspect ratio distribution function. In practice, it is more convenient to determine the aspect ratio distribution in terms of crack porosity. According to Eq. (2), the porosity of cracks in the same range is given by $d\phi \approx (4\pi\alpha/3)\gamma(\alpha)d\Gamma$. The *aspect ratio distribution function of crack porosity* is then written as:

$$f(\alpha) = \frac{d\phi}{d\alpha} = \frac{4\pi\alpha}{3}\gamma(\alpha) \tag{3}$$

3.2. Crack closure and elastic nonlinearity

The 3D penny-shaped micro-cracks (or oblate ellipsoidal pores) induced by heat-treatment can be closed under a given hydrostatic compression stress, depending on the crack initial aspect ratio α. Due to this, the progressive closure of micro-cracks with different aspect ratios leads to nonlinear elastic response of the material, which is observed experimentally by the evolution of $K_b = (1/C_{bc})$ with P_c, see Section 2.3.

At given aspect ratio α, pore compressibility C_{pc}, defined with respect to initial pore volume V_{p0}, is assumed constant: $\Delta V_p/V_{p0} = -C_{pc}\Delta P_c$. The pore closes at a hydrostatic pressure $P^* = \Delta P_c$ such that its volume variation $-\Delta V_p$ is equal to its initial volume V_{p0}. Therefore, the closing pressure P^* of a three-dimensional penny-shaped crack of initial aspect ratio α is $P^* = (1/C_{pc})$. For a single 3D penny-shaped crack, isolated in an infinite medium and subjected to hydrostatic pressure at infinity, with thin opening (small values of α), it is shown that ([18]):

$$C_{pc} = \frac{2(1-\nu_m)}{\pi\alpha G_m} \tag{4}$$

where ν_m is the matrix Poisson ratio and G_m is the matrix shear modulus. Using that $3(1-2\nu_m)/C_m = 2G_m(1+\nu_m)$, where C_m is the matrix compressibility, Eq. (4) becomes:

$$C_{pc} = \frac{4(1-\nu_m^2)}{3\pi\alpha(1-2\nu_m)}C_m \tag{5}$$

Therefore, the closing pressure of a 3D penny-shaped crack of initial aspect ratio α is:

$$P^* = \frac{1}{C_{pc}} = \frac{3\pi(1-2\nu_m)}{4(1-\nu_m^2)C_m}\alpha \tag{6}$$

This means that at given hydrostatic pressure P, open cracks have an initial aspect ratio α greater or equal to $4(1-\nu_m^2)C_mP/(3\pi(1-2\nu_m))$. Elastic strain energy considerations ([18]) show that:

$$\frac{1}{K_b} = C_{bc} = C_m + \phi C_{pc} \tag{7}$$

Substituting Eqs. (2) and (5) into Eq. (7), one gets:

$$C_{bc} = C_m\left(1 + \frac{16(1-\nu_m^2)}{9(1-2\nu_m)}\Gamma\right) \tag{8}$$

Eq. (8) shows that bulk compressibility C_{bc} is independent of initial aspect ratio α: it only depends upon crack-density parameter Γ. Moreover, the chain rule gives:

$$\frac{dC_{bc}}{dP} = \frac{dC_{bc}}{d\Gamma}\frac{d\Gamma}{d\alpha}\frac{d\alpha}{dP} \tag{9}$$

where $dC_{bc}/d\Gamma$ is provided by differentiating Eq. (8), and $d\alpha/dP$ is provided by differentiating Eq. (6), both for P tending towards P^*, i.e. for cracks on the verge of closing. Finally:

$$\frac{dC_{bc}}{dP} = \frac{dC_{bc}}{d\Gamma}\frac{d\Gamma}{d\alpha}\frac{d\alpha}{dP} = \frac{4\pi}{3}\left[\frac{4(1-\nu_m^2)C_m}{3\pi(1-2\nu_m)}\right]^2\frac{d\Gamma}{d\alpha} \tag{10}$$

Determining the aspect ratio distribution function of crack porosity $f(\alpha) = -(4\pi\alpha/3)(d\Gamma/d\alpha)$ now reduces to determining (dC_{bc}/dP). This is performed using experimental data, by fitting a smooth curve to $C_{bc}(P)$ in order to avoid numerical instabilities. Former works by ([18,22,35]) propose the following exponential relation:

$$C_{bc} = C_{bc}^{\infty} + \left(C_{bc}^{i} - C_{bc}^{\infty}\right)e^{-P/\widehat{P}} \tag{11}$$

where C_{bc}^{i} is the compressibility at zero pressure, while C_{bc}^{∞} is the asymptotic compressibility which is reached at very high pressure when all the cracks are closed. $\widehat{P}$ is a characteristic (crack-closing) pressure defining the kinetics of compressibility variation.

Differentiating Eq. (11) with respect to P, and replacing $\widehat{P}$ by $\hat{\alpha}$ (resp. P by α) using Eq. (6), yields:

$$\gamma(\alpha) = -(d\Gamma/d\alpha) = \left[\frac{9(1-2\nu_m)}{16(1-\nu_m^2)C_m}\right]\frac{\left(C_{bc}^{i} - C_{bc}^{\infty}\right)}{\hat{\alpha}}e^{-\alpha/\hat{\alpha}} \tag{12}$$

The aspect ratio distribution function of crack porosity is written as:

$$f(\alpha) = \frac{4\pi\alpha}{3}\gamma(\alpha) = \frac{3\pi(1-2\nu_m)}{4(1-\nu_m^2)}\frac{\left(C_{bc}^{i} - C_{bc}^{\infty}\right)}{C_m}\frac{\alpha}{\hat{\alpha}}e^{-\alpha/\hat{\alpha}} \tag{13}$$

The total crack porosity ϕ is then calculated by integrating $f(\alpha)$ over all values of α, from 0 to ∞:

$$\phi = \int_0^{\infty} f(\alpha)d\alpha = \frac{3\pi(1-2\nu_m)}{4(1-\nu_m^2)}\frac{\left(C_{bc}^{i} - C_{bc}^{\infty}\right)}{C_m}\hat{\alpha} = \left(C_{bc}^{i} - C_{bc}^{\infty}\right)\widehat{P} \tag{14}$$

3.3. Experimental identification and model predictions

For the mortar studied here, pure silica sand is used and it is composed of tiny elements (d = 0–1 mm), medium (d = 1–1.6 mm) and large ones (d = 1–6.2 mm). The average diameter of grains is d_{mean} = 1.3 mm. As presented in Section 3.1, the average radius a of micro-cracks is considered uniform. For mortar, this crack radius is taken as equal to the average radius of sand grains: $a \approx r(sand)$ = 0.65 mm. Indeed, the heat-induced micro-cracks, considered here as elements of the so-called microscale, are similar to those observed by Fu et al. [3,4] at the interface between sand grains and cement paste. They are assumed of greater order of magnitude than cement paste capillary pores.

Experimental identification of the micro-mechanical model consists mainly in determining the parameters $C_{bc}^{i}, C_{bc}^{\infty}$ and $\widehat{P}$ (or rather $\hat{\alpha}$) involved in Eq. (11). For each heat-treatment temperature T, the initial bulk compressibility, $C_{bc}^{i} = 1/K_b$ is determined as the initial slope of volumetric strain data at the beginning of hydrostatic compression (when hydrostatic pressure tends towards zero). For the asymptotic compressibility, C_{bc}^{∞}, at very high hydrostatic pressure, it corresponds physically to the compressibility after all heating-induced cracks are closed. Therefore, we assume that asymptotic compressibility C_{bc}^{∞} is the compressibility of reference material, i.e. $C_{bc}^{\infty} = 1/K_b(ref.)$. Note that $K_b(ref.)$ is determined from the mortar dried at 60 °C, and at such temperature the heating-induced micro-cracks are assumed negligible. Further, the compressibility of the solid matrix C_m has been assessed in former work, see [11]. It is taken at a constant value, independent of heat-treatment temperature T: $C_m = 1/K_m(ref.) = 1/(45.1\ \text{GPa}) = 0.022(1/\text{GPa})$. Note that due to complex micro-structure of mortar, the compressibility of solid matrix C_m includes that of occluded pores. Due to its reputed low influence on the results, see [18], matrix Poisson ratio ν_m is taken at a constant value of 0.15, independently of T, as in [12].

The variation of bulk compressibility C_{bc} with confining pressure $P = P_c$ is calculated using Eq. (11) and it is positively compared with experimental data, see Fig. 2. Due to progressive closure of micro-cracks of different aspect ratios, compressibility curves are

Table 4
Compressibility parameters for mortar heat-treated up to different temperatures *T*.

Mortar type	K_b ($P_c = 0$) (GPa)	C_{bc}^{i} (1/GPa)	C_{bc}^{∞} (1/GPa)	C_m (1/GPa)	ν_m	$\widehat{P}$ (MPa)	$\hat{\alpha}$	ϕ (%)
Reference	16.3	0.061	0.061	0.022	0.15	–	–	0.00
200 °C	11.61	0.086	0.061	0.022	0.15	33.72	0.44×10^{-3}	0.08
300 °C	7.42	0.135	0.061	0.022	0.15	26.64	0.35×10^{-3}	0.20
400 °C	6.25	0.160	0.061	0.022	0.15	25.22	0.33×10^{-3}	0.25

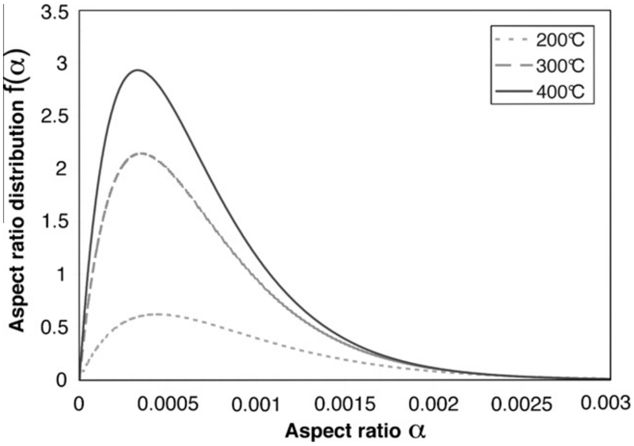

Fig. 4. The aspect ratio distribution functions $f(\alpha)$ for mortar heat-treated at different temperatures *T*.

described by decreasing functions of the confining pressure. Mortar heat-treated at higher temperature is more sensitive to hydrostatic stress P_c. All identified parameters for mortar treated at different temperatures are given in Table 4. We can see that the initial bulk modulus C_{bc}^{i} decreases significantly with heat-treatment temperature *T* due to the presence of more and more micro-cracks; the characteristic aspect ratio ($\hat{\alpha}$) slightly decreases with temperature *T*. $f(\alpha)$ is plotted for different heat-treatment temperatures in Fig. 4. The total crack porosity ϕ, which is the area under the $f(\alpha)$ curves, increases significantly with heat-treatment temperature. $\hat{\alpha}$ is the maximum (or peak) value of the aspect ratio distribution function of crack porosity $f(\alpha)$: it decreases only slightly with increasing heat-treatment temperature, meaning that the higher the heat-treatment, the more numerous, but the smaller, the micro-cracks.

As shown in Fig. 5a, the heating-induced crack porosity ϕ is well correlated with the significant increase of material intrinsic permeability. Although limited in number, the data points (ϕ,K_{int}) follow an exponential evolution with a Pearson's correlation coefficient as high as 97%: $K_{int}/K_0 = 0.9 \times \exp(13.06\ \phi)$.

Normalized permeability may also be plotted as a function of aspect ratio α, using Eq. (6). For all heat-treatment temperatures $T \geqslant 60$ °C, a *single* fitting with an exponential law is found: $K_{int}/K_0 = 1.05 \times \exp(-1030\ \alpha)$, with a very good Pearson's correlation coefficient of 99%.

3.4. Determination of stress–strain curves

In conjunction with the micro-mechanical analysis of poro-elastic and transport properties of heat-treated mortar, we propose to determine macroscopic stress–strain curves using both bulk compressibility evolution and a phenomenological law. By definition of the elastic bulk compressibility C_{bc}, the elastic strain can be calculated by:

$$\varepsilon_v^{el} = \int_0^{P_c} d\varepsilon_v^{el} = \int_0^{P_c} \frac{dP_c}{K_b} = \int_0^{P_c} C_{bc} dP \tag{15}$$

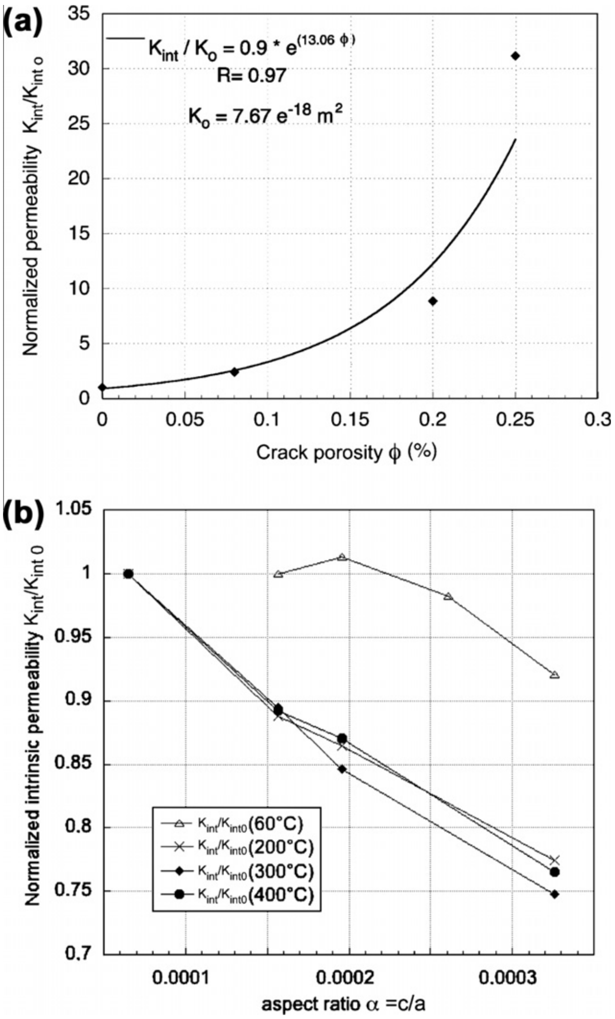

Fig. 5. Correlation between (a) normalized intrinsic permeability K_{int}/K_{int0} and heating-induced crack porosity ϕ; (b) normalized intrinsic permeability with aspect ratio α. K_{int0} is the intrinsic permeability of reference mortar at 5 MPa confinement.

As shown in Fig. 1 and in previous work [11], heat-treated mortar presents plastic (irreversible) strains upon complete unloading, whenever confining pressure exceeds a certain threshold. This plastic deformation is mainly attributed to irreversible collapse of pores (and of solid skeleton bridges) under hydrostatic stress. Based on experimental data, the following phenomenological linear relationship is proposed to relate hydrostatic stress P_c and plastic volumetric strain ε_v^{pl}:

$$P_c = P_0\left[1 + m\varepsilon_v^{pl}\right] \tag{16}$$

Parameters P_0 and m define respectively the threshold of plastic pore collapse and the rate of plastic volumetric compaction. Physically, both parameters are related to the state of micro-cracks induced by heat-treatment, and should depend on *T*. However, according to our experimental data, in first instance, the variation

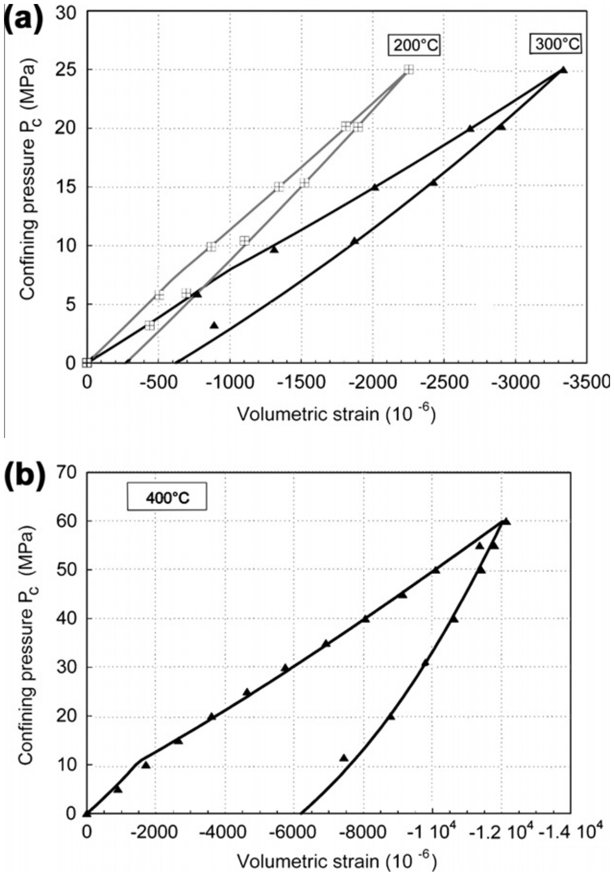

Fig. 6. Comparison between numerical calculations (continuous lines) and test data (points) for samples heated up to (a) 200 and 300 °C (first series of poro-mechanical tests), or (b) 400 °C (second series).

of P_0 is limited to 16% of its average, so that an average value is used for all heat-treatment temperatures T: $P_0 = 8.5$ MPa. On the other hand, the value of m decreases significantly with temperature T: it is equal to 8840, 3620 and 747, respectively for samples heat-treated up to 200, 300 and 400 °C. This means that the plastic deformation rate $\left(d\varepsilon_v^{pl} = \frac{dP_c}{m.P_0}\right)$ is higher with increasing heat-treatment temperature T and that the mortar becomes more ductile with T.

By adding elastic and plastic strains, the total strain of mortar is calculated as a function of hydrostatic stress P_c. Calculations are compared with experimental data in Fig. 6a and b. Note that the experimental data plotted in Fig. 6b are the average values of two tests performed on two different samples (for details on laboratory tests, see [11]). We observe that the mechanical response becomes less and less linear with increasing heat-treatment temperature T. Plastic deformation increases with T. There is good agreement between model predictions and test data. The proposed model predicts correctly both elastic and plastic deformation of mortar.

4. Conclusions

This work is based on hydrostatic compression tests performed on mortar preliminarily subjected to a heat-treatment (slow heating/cooling process) up to different temperatures $T = 200$, 300 or 400 °C. Experimental results both show nonlinearities and irreversibilities in the stress–strain curves, together with a significant increase in gas permeability with T, for the same material. This is mainly attributed to heating-induced micro-cracking.

A micro-mechanical analysis is proposed to describe the effect of heating-induced micro-cracks upon both poro-elastic properties and intrinsic gas permeability. The micro-mechanical model shows that there is an increasing amount of micro-cracks with increasing heat-treatment temperature T, with an aspect ratio distribution of crack porosity slightly switching to smaller micro-cracks. Further, the heating-induced crack porosity ϕ is clearly correlated with the increase in mortar intrinsic permeability. Alternately, intrinsic permeability is very well correlated with crack aspect ratio: the higher the initial crack aspect ratio, the higher the permeability.

The overall mechanical response of heat-treated mortar under hydrostatic compression was also investigated. Due to the increasing amount of micro-cracks induced by heat-treatment, the mechanical response of mortar becomes less and less linear with T, and exhibits important plastic compaction, mainly attributed to the progressive closure of micro-cracks and to irreversible pore collapse. A constitutive model is proposed, based on both the micro-mechanical analysis and on a phenomenological approach. There is good agreement between numerical predictions and experimental data. The proposed model is able to describe both elastic and plastic strains by taking into account heating-induced micro-cracks.

References

[1] Chen XT, Rougelot Th, Davy CA, Chen W, Agostini F, Skoczylas F, et al. Experimental evidence of a moisture clog effect in cement-based materials under temperature. Cement Concrete Res 2009;39:1139–48.
[2] Rostasy RS, Weiss R, Wiedemann G. Changes of pore structure of cement mortar due to temperatures. Cement Concrete Res 1980;10:157–64.
[3] Fu YF, Wong YL, Tang CA, Poon CS. Thermal induced stress and associated cracking in cement-based composite at elevated temperatures-part ii: thermal cracking around multiple inclusions. Cement Concrete Compos 2004;26: 113–26.
[4] Fu YF, Wong YL, Poon CS, Tang CA, Lin P. Experimental study of micro/macro crack development and stress–strain relations of cement-based composite materials at elevated temperatures. Cement Concrete Res 2004;34:789–97.
[5] Peng GF. Evaluation of fire damage to high performance concrete. PhD Thesis, The Hong Kong Polytechnic University, Hong Kong; 1999.
[6] Taylor HFW. Cement chemistry. 2nd ed. London: Telford Publishing; 1997.
[7] Noumowé A. Effet des hautes températures (20–600 °C) sur les bétons, cas particulier du béton à hautes performances. In Thèse de doctorat (PhD Thesis, in French); 1995.
[8] Castellote M, Alonso C, Andrade C, Turrillas X. Composition and microstructural changes of cement pastes upon heating, as studied by neutron diffraction. Cement Concrete Res 2004;34:1633–44.
[9] Cruz CR, Gillen M. Thermal expansions of portland cement paste, mortar and concrete at high temperature. Fire Mater 1980;4:66–70.
[10] Hearn N. Effect of shrinkage and load-induced cracking on water permeability of concrete. ACI Mater J 1999;96(2):234–41.
[11] Chen XT, Davy CA, Skoczylas F, Shao JF. Effect of heat-treatment and hydrostatic loading upon the poro-elastic properties of a mortar. Cement Concrete Res 2009;39:195–205.
[12] Chen XT, Shao JF, Davy CA, Skoczylas F. Experimental study and elastoplastic damage modeling of mortar with thermal effects. Int J Numer Anal Methods Geomech 2009.
[13] Lemaitre J. A course on damage mechanics. Berlin: Springer-Verlag; 1992.
[14] Mazars J, Pijaudier-Cabot G. Continuum damage theory – application to concrete. J Eng Mech ASCE 1989;115(2):345–65.
[15] Dal Pont S, Schrefler BA, Ehrlacher A. Experimental and finite element analysis of a hollow cylinder submitted to high temperatures. Mater Struct 2005;38:681–90.
[16] Gawin D, Majorana CE, Schrefler BA. Numerical analysis of hygro-thermal behaviour and damage of concrete at high temperature. Mech Cohes-Frict Mater 1999;4:37–74.
[17] Selvadurai APS. Stationary damage modelling of poroelastic contact. Int J Solids Struct 2004;41:2043–64.
[18] Zimmerman RW. Compressibility of sandstones. Amsterdam, The Netherlands: Elsevier; 1991.
[19] Deudé V, Dormieux L, Kondo D, Pensée V. Propriétés élastiques nonlinéaires d'un milieu mésofissuré. C R Mec 2002;330:587–92.
[20] Dormieux L, Kondo D. Approche micromécanique du couplage perméabilité-endommagement. C R Mec 2004;332:135–40.
[21] Walsh JB. The effect of cracks on the compressibility rocks. J Geophys Res 1965;70(2):381–9.
[22] Morlier P. Description de l'état de fissuration d'une roche à partir d'essais non-destructifs simples (description of the state of rock fracturization through simple non-destructive tests). Rock Mech 1971;3(3):125–38.

[23] Deudé V, Dormieux L, Kondo D, Maghous S. Micromechanical approach to nonlinear poroelasticity: application to cracked rocks. J Eng Mech 2002;128(8):0733–9399.

[24] Yurtdas I, Burlion N, Skoczylas F. Experimental characterization of the drying effect on uniaxial mechanical behaviour of mortar. Mater Struct 2004;37(267):170–6.

[25] Lion M, Skoczylas F, Lafhaj Z, Sersar M. Experimental study on a mortar. temperature effects on porosity and permeability. residual properties or direct measurements under temperature. Cement Concrete Res 2005;35:1937–42.

[26] Colina H, Acker P. Drying cracks: kinematics and scale laws. Mater Struct 2000;33:101–7.

[27] Gaweska-Hager I. Comportement à haute température des bétons à haute performance – évolution des principales propriétés mécaniques. Thèse de Doctorat (PhD Thesis, in French), Ecole Nationale des Ponts et Chaussées/Ecole Polytechnique de Cracovie, France; 2004.

[28] Menou A. Etude du comportement thermomécanique des bétons à haute température: approche multi-échelles de l'endommagement thermique. In Thèse de doctorat de l'Université de Pau et des Pays de l'Adour (PhD Thesis, in French); 2004.

[29] Coussy O. Poromechanics. New York: J. Wiley & Sons; 2004.

[30] Klinkenberg LJ. The permeability of porous media to liquids and gases. Drilling and Production Practice, American Petroleum Institute; 1941. p. 200–13.

[31] Loosveldt H, Lafhaj Z, Skoczylas F. Experimental study of gas and liquid permeability of a mortar. Cement Concrete Res 2002;32:1357–63.

[32] Kherbouche R. Etude du comportement poro-élasto-plastique de la craie. Thèse de Doctorat (PhD Thesis, in French), Université des Sciences et Technologies de Lille, France; 1994.

[33] Dormieux L, Kondo D, Ulm FJ. Microporomechanics. John Wiley and Sons Ltd.; 2006.

[34] Dormieux L, Lemarchand E, Kondo D, Fairbairn E. Elements of poro-micromechanics applied to concrete. Mater Struct 2004;37:31–42.

[35] Wyble DO. Effect of applied pressure on the conductivity, porosity, and permeability of sandstones. Petrol Trans AIME 1958;213:430–2.